Analysis and Control Design of a Step-Up/Step-Down Converter for Battery-Discharge Voltage Regulation

Juan A Villanueva-Loredo, Panfilo R Martinez-Rodriguez, Christopher J Rodriguez-Cortés, Diego Langarica-Cordoba, Ángel Hernández-Gómez, Damien Guilbert

▶ **To cite this version:**

Juan A Villanueva-Loredo, Panfilo R Martinez-Rodriguez, Christopher J Rodriguez-Cortés, Diego Langarica-Cordoba, Ángel Hernández-Gómez, et al.. Analysis and Control Design of a Step-Up/Step-Down Converter for Battery-Discharge Voltage Regulation. Electronics, 2025, 14 (5), pp.877. ⟨10.3390/electronics14050877⟩. ⟨hal-04962591⟩

HAL Id: hal-04962591

https://hal.science/hal-04962591v1

Submitted on 23 Feb 2025

HAL is a multi-disciplinary open access archive for the deposit and dissemination of scientific research documents, whether they are published or not. The documents may come from teaching and research institutions in France or abroad, or from public or private research centers.

L'archive ouverte pluridisciplinaire **HAL**, est destinée au dépôt et à la diffusion de documents scientifiques de niveau recherche, publiés ou non, émanant des établissements d'enseignement et de recherche français ou étrangers, des laboratoires publics ou privés.

Distributed under a Creative Commons CC BY 4.0 - Attribution - International License

electronics

MDPI

Article

Analysis and Control Design of a Step-Up/Step-Down Converter for Battery-Discharge Voltage Regulation

Juan A. Villanueva-Loredo [1], Panfilo R. Martinez-Rodriguez [1], Christopher J. Rodriguez-Cortés [1], Diego Langarica-Cordoba [1], Ángel Hernández-Gómez [1] and Damien Guilbert [2,*]

[1] School of Sciences, Universidad Autónoma de San Luis Potosí (UASLP), San Luis Potosí 78295, Mexico; juan.villanueva@uaslp.mx (J.A.V.-L.); panfilo.martinez@uaslp.mx (P.R.M.-R.); cjrcortes@ieee.org (C.J.R.-C.); diego.langarica@uaslp.mx (D.L.-C.); angel.hernandez@uaslp.mx (Á.H.-G.)

[2] Groupe de Recherche en Electrotechnique et Automatique du Havre (GREAH), Université Le Havre Normandie, 75 Rue Bellot, P.C. 76600 Le Havre, France

* Correspondence: damien.guilbert@univ-lehavre.fr

Abstract: In recent years, step-up/step-down DC–DC converters have been required in renewable energy processing and energy storage applications. In the latter, lithium-ion batteries have played an important role since they have been the most usable source in portable equipment and electric vehicles. This paper proposes a novel step-up/step-down converter with continuous input current and a model-based control scheme. Moreover, the converter design highlights based on steady-state analysis are obtained for a proper parameter selection of the converter. Thus, a fourth-order average system model is obtained to design a multiloop control law. The proposed control is designed in such a way that the control scheme results in an inner current loop on the input current and an outer control loop on the output voltage. Finally, experimental results are performed to assess the performance of the proposed power converter and the control law. An experimental setup with an efficiency of 95 % is implemented to validate the theoretical analysis. The intended application is to regulate a voltage fluctuation from 200 V to 250 V to a constant voltage of 200 V with a nominal power of 533 W.

Keywords: switching regulator; buck–boost converter; step-down/up converter; lithium-ion battery pack; non-pulsating input current; two-loop control

check for updates

Academic Editors: Mingrui Leng, Qingxin Tian and Yuan Li

Received: 3 December 2024
Revised: 5 February 2025
Accepted: 20 February 2025
Published: 23 February 2025

Citation: Villanueva-Loredo, J.A.; Martinez-Rodriguez, P.R.; Rodriguez-Cortés, C.J.; Langarica-Cordoba, D.; Hernández-Gómez, Á.; Guilbert, D. Analysis and Control Design of a Step-Up/Step-Down Converter for Battery-Discharge Voltage Regulation. *Electronics* **2025**, *14*, 877. https://doi.org/10.3390/electronics14050877

Copyright: © 2025 by the authors. Licensee MDPI, Basel, Switzerland. This article is an open access article distributed under the terms and conditions of the Creative Commons Attribution (CC BY) license (https://creativecommons.org/licenses/by/4.0/).

1. Introduction

Environmental pollution is a worldwide problem; one of the main concerns around the problem is the global warming produced mainly by the CO_2 emissions of fossil-fuel burning. Significant efforts have been dedicated to studying and implementing renewable energy sources to reduce fossil-fuel dependence. Energy harvesting from fuel cells, wind turbines, or photovoltaic panels is the most promising environmentally friendly solution; this energy can be sent directly to the grid or stored in batteries. For these applications, the use of DC–DC converters is mandatory to process energy between the renewable energy source, the grid, the battery, and the load. A step-up converter is used when the voltage level needs to be increased; on the other hand, a step-down converter is used when a voltage reduction is required. However, in recent years, many applications require both features, making use of step-up/step-down converters necessary. For instance, in [1,2], step-up/step-down converters are proposed to regulate the DC voltage from a photovoltaic panel to a suitable DC bus to connect a DC–AC inverter. Furthermore, in [3], a buck–boost converter with an extended buck region is proposed as an attractive solution to track

the maximum power points in renewable energy resources. Additionally, in [4], after a diode bridge, a single-stage step-up/step-down converter is proposed as a PFC source for LED lamps. Also, in [5], a conventional buck–boost topology with anti-interference control is proposed to provide power to loads in a microgrid. A novel application for step-up/step-down converters is the charging or discharging battery systems for portable devices and electric vehicles. In [6], a buck–boost series partial power converter is used as a DC voltage regulator for an electric vehicle charging station. Also, in [7], a modified buck–boost converter is proposed to track sinusoidal signals in an exact form for UPS system applications. In [8], a bidirectional buck–boost is proposed to charge a battery from a PV panel and discharge the battery to a portable load. Moreover, in [9], a multi-output buck–boost converter is proposed to obtain several available voltage levels using a battery as a source for electric vehicle applications.

Lithium-ion batteries are used as a power source in portable devices because they have high energy density. However, each battery cell has a voltage fluctuation from 4.2 V when fully charged to 2.7 V when discharged [10], as shown in Figure 1. Thus, an interface based on a DC–DC step-down/step-up converter is required to maintain the output voltage regulated to a desired average value between the battery and its load [11]; a scheme for this application is shown in Figure 2. For instance, in [12], a step-up/step-down converter with flying capacitors is proposed to regulate the voltage of a battery cell to 3.4 V. In [13], a non-inverting buck–boost converter is proposed to regulate 3.6 V from a lithium-ion battery to power an LED light. In addition, in [14], a step-up/down converter is proposed to regulate a fluctuation voltage range of the battery of 40–56 V to a nominal voltage of 48 V. Furthermore, it is also recommended that lithium-ion batteries do not present periodic pulse current profiles when they are discharged because these abrupt changes are detrimental [15]. In this intended application, the output current of the battery is equal to the input current of the converter, as seen in Figure 1. Therefore, the converter must feature a non-pulsating input current, i.e., that the current does not change from one value to another abruptly, which is achieved through an input inductor at the converter since it maintains a continuous current.

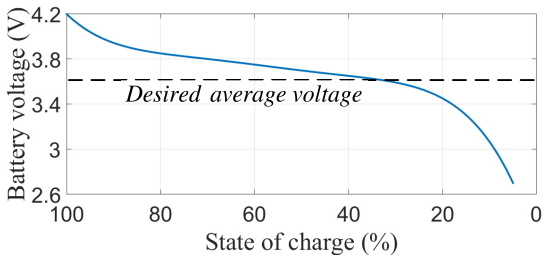

Figure 1. Battery voltage according to the state of charge.

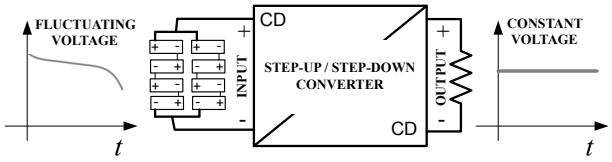

Figure 2. Voltage regulation of Li–ion batteries.

Therefore, the main goal of this type of system is to keep the output voltage regulated to the desired voltage reference on average, as shown in Figure 2. Several step-down/step-up converters, previously reported in the literature, can fulfill this objective. The conventional buck–boost converters have few components; however, their output voltage is inverted, and this disadvantage makes it difficult to connect the converter with other

subsystems [15]. The Cúk converter has the same drawback. Non-inverting step-up/step-down converters with high efficiency are reported in [16–18]; however, their input current behavior is pulsating, which is not recommended for batteries. There are non-inverting step-up/step-down converters with non-pulsating input current, for instance, the SEPIC converter [1,11,14,19,20]. However, the SEPIC converter exhibits high current and voltage stress in semiconductors [21]. The same problem is observed in the converters reported in [11,14,19]. These converters have structures with many components affecting the power density. In [1,20], quadratic converters with a high conversion ratio are presented. Nevertheless, this benefit is not exploited because a voltage gain of $D/(1-D)$ is enough to reach the voltage levels for the intended application. The use of a transformerless DC–DC converter in battery voltage regulation is desirable since isolated topologies contain a transformer, which increases costs and reduces the power density of the converter. Isolated topologies are commonly used in battery chargers to electrically isolate the battery from the grid for normative and safety reasons [22]. Another possible solution is a cascaded interconnection of a boost in the first stage and a buck in the second stage. Nevertheless, this approach compromises efficiency. Non-cascading structures of two stages called reduced redundant power processing converters are studied in [23]; here, part of the power is processed only by one stage, making them more efficient than cascading converters.

In this paper, a new step-up/step-down topology is proposed. This is able to regulate the output voltage on average to the desired reference considering an input fluctuating voltage with application to lithium-ion battery cells. The proposed structure is shown in Figure 3. Hence, the main contributions are the following:

1. A non-pulsating step-up/step-down converter is proposed. Notice that the input current is continuous due to the location of the input inductor L_1.
2. The converter has a non-inverting output voltage with a common ground.
3. The number of switches is low compared with other step-up/step-down converters.
4. The input source and load are both connected to the same ground level.
5. The structure reduces redundant power processing, increasing the efficiency, i.e., according to [23], it is a non-cascading structure.
6. A procedure design for the energy storage elements is proposed to select the capacitances and inductances.
7. For the proposed step-up/step-down converter, a fourth-order bilinear model of the system is obtained, and a model-based control is proposed. Moreover, a linearized version of the non-linear model is obtained to encourage future applications of the converter.

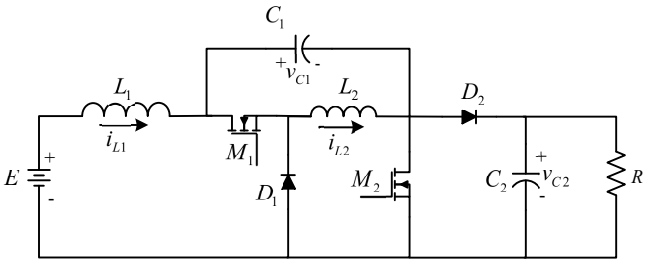

Figure 3. Proposed step–up/step–down converter.

The rest of the paper is organized as follows: Section 2 describes the modeling process to obtain the non-linear and linear models from the equivalent operation modes of the converter. Expression of nominal average values of the state variables, ripples, and current and voltage stress in semiconductors are deduced in Section 3. The control scheme is analyzed in Section 4. Experimental results of a prototype up to 533 W as well as an

efficiency analysis and a comparison with other converters are carried out in Section 5. Finally, concluding remarks are given in Section 6.

2. Modeling and System Description

In this section, the proposed converter is analyzed. The analysis includes its ripple waveforms, mathematical models, equilibrium operation point, stress component values in semiconductors, and ripple expressions for passive component selection. The proposed converter shown in Figure 3 is composed of an input inductor L_1, an output inductor L_2, a transfer capacitor C_1, an output capacitor C_2, two active switches M_1 and M_2, two diodes D_1 and D_2, a load R and an input voltage E as power source.

The converter analysis considers the operation in Continuous Conduction Mode (CCM) with the active switches operating with the same duty cycle signal, i.e., synchronously. Thus, two operation modes appear; mode 1 is the equivalent circuit when the active switches turn on, shown in Figure 4a; mode 2 is the equivalent circuit when the active switches turn off, shown in Figure 4b. It can be noticed that in mode 2, the current supplied by the source i_{L1} reaches the output node in parallel with the current i_{L2}, which is a reduced redundant power processing feature [23] which makes the proposed converter a non-cascading structure. There are four state variables: the inductor currents i_{L1} and i_{L_2}, and the capacitor voltages v_{C1} and v_{C2}. The behavior of the system during mode 1 is described as,

$$L_1\frac{di_{L1}}{dt} = -v_{C1} + E, \tag{1}$$

$$L_2\frac{di_{L2}}{dt} = v_{C1}, \tag{2}$$

$$C_1\frac{dv_{C1}}{dt} = i_{L1} - i_{L2}, \tag{3}$$

$$C_2\frac{dv_{C2}}{dt} = -\frac{v_{C2}}{R}. \tag{4}$$

On the other hand, the system during mode 2 is described as,

$$L_1\frac{di_{L1}}{dt} = -v_{C1} - v_{C2} + E, \tag{5}$$

$$L_2\frac{di_{L2}}{dt} = -v_{C2}, \tag{6}$$

$$C_1\frac{dv_{C1}}{dt} = i_{L1}, \tag{7}$$

$$C_2\frac{dv_{C2}}{dt} = i_{L1} + i_{L2} - \frac{v_{C2}}{R}. \tag{8}$$

Using a binary switching function q, we can join the differential equations of mode 1 and mode 2: q has the value of 1 when the active switches are turned on (mode 1); q has the value of 0 when the active switches are turned off (mode 2). Thus, the fourth-order bilinear switching model is represented as,

$$L_1\frac{di_{L1}}{dt} = -v_{C1} - (1-q)v_{C2} + E, \tag{9}$$

$$L_2\frac{di_{L2}}{dt} = qv_{C1} - (1-q)v_{C2}, \tag{10}$$

$$C_1\frac{dv_{C1}}{dt} = i_{L1} - qi_{L2}, \tag{11}$$

$$C_2\frac{dv_{C2}}{dt} = (1-q)i_{L1} + (1-q)i_{L2} - \frac{v_{C2}}{R}. \tag{12}$$

Considering the average value of q, denoted by the duty cycle d, a non-linear average model can be derived, yields in,

$$\frac{di_{L1}}{dt} = -\frac{1}{L_1}v_{C1} - \frac{1-d}{L_1}v_{C2} + \frac{E}{L_1}, \tag{13}$$

$$\frac{di_{L2}}{dt} = \frac{d}{L_2}v_{C1} - \frac{1-d}{L_2}v_{C2}, \tag{14}$$

$$\frac{dv_{C1}}{dt} = \frac{1}{C_1}i_{L1} - \frac{d}{C_1}i_{L2}, \tag{15}$$

$$\frac{dv_{C2}}{dt} = \frac{1-d}{C_2}i_{L1} + \frac{1-d}{C_2}i_{L2} - \frac{1}{C_2R}v_{C2}. \tag{16}$$

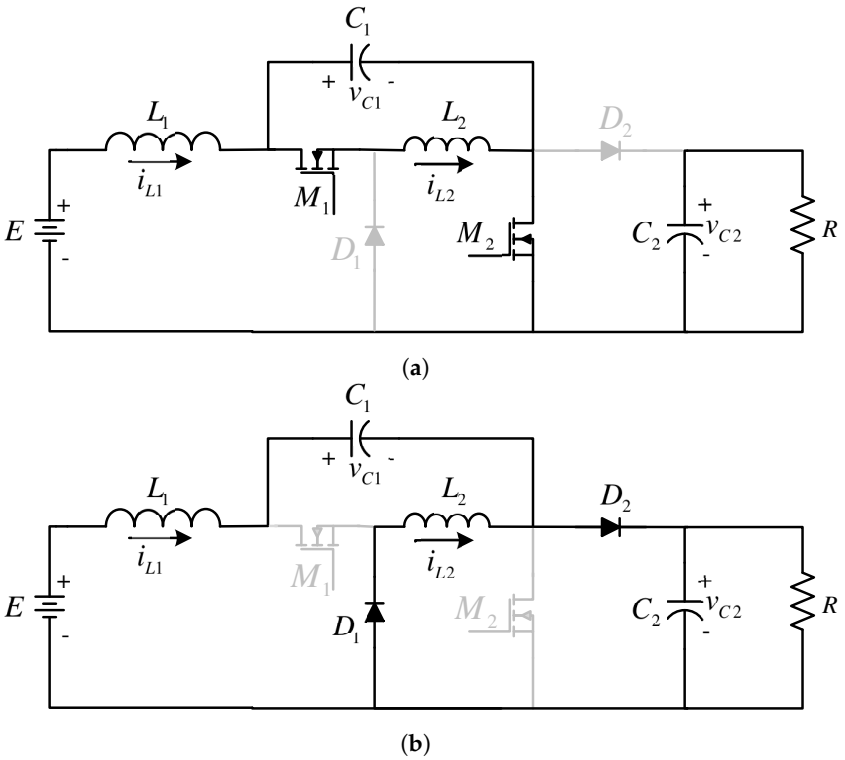

Figure 4. Equivalent circuits of the proposed converter. (**a**) Operation mode 1: active switches turned on. (**b**) Operation mode 2: active switches turned off.

The state variables i_{L1}, i_{L2}, v_{C1}, and v_{C2} of the average model (13)–(16) can be decomposed into its nominal DC values and the small-signal AC component. The DC nominal value is represented with upper-case letters; meanwhile, the AC component is represented by the superscript $\sim$ as is shown,

$$i_{L1} = I_{L1} + \tilde{i}_{L1}, \tag{17}$$

$$i_{L2} = I_{L2} + \tilde{i}_{L2}, \tag{18}$$

$$v_{C1} = V_{C1} + \tilde{v}_{C1}, \tag{19}$$

$$v_{C2} = V_{C2} + \tilde{v}_{C2}, \tag{20}$$

$$d = D + \tilde{d}. \tag{21}$$

A linearized small AC signal model can be derived by replacing the decomposed values expressed in (17)–(21) in the non-linear average model obtained in (13)–(16) around the equilibrium point corresponding to the nominal DC values, which yields

$$\frac{d\tilde{i}_{L1}}{dt} = -\frac{1}{L_1}\tilde{v}_{C1} - \frac{1-D}{L_1}\tilde{v}_{C2} + \frac{ED}{(1-D^2)L_1}\tilde{d}, \tag{22}$$

$$\frac{d\tilde{i}_{L2}}{dt} = \frac{D}{L_2}\tilde{v}_{C1} - \frac{1-D}{L_1}\tilde{v}_{C2} + \frac{E}{(1-D^2)L_2}\tilde{d}, \tag{23}$$

$$\frac{d\tilde{v}_{C1}}{dt} = \frac{1}{C_1}\tilde{i}_{L1} - \frac{D}{C_1}\tilde{i}_{L2} + \frac{ED}{(1-D^2)^2RC_1}\tilde{d}, \tag{24}$$

$$\frac{d\tilde{v}_{C2}}{dt} = \frac{1-D}{C_2}\tilde{i}_{L1} + \frac{1-D}{C_2}\tilde{i}_{L2} - \frac{1}{C_2R}\tilde{v}_{C2} + \frac{ED}{(1+D)(1-D)^2RC_2}\tilde{d}. \tag{25}$$

Furthermore, the transfer functions $\tilde{i}_{L1}/\tilde{d}$ and $\tilde{v}_{C2}/\tilde{d}$ are obtained from the linear model (9)–(12), resulting in

$$\frac{\tilde{i}_{L1}}{\tilde{d}} = \frac{b_3s^3 + b_2s^2 + b_1s^1 + b_0}{s^4 + a_3s^3 + a_2s^2 + a_1s^1 + a_0}, \tag{26}$$

and

$$\frac{\tilde{v}_{C2}}{\tilde{d}} = \frac{c_3s^3 + c_2s^2 + c_1s^1 + c_0}{s^4 + a_3s^3 + a_2s^2 + a_1s^1 + a_0}, \tag{27}$$

where the value of each coefficient is expressed in Table 1. Notice that c_1 and c_3 are negative constants and consequently (27) exhibit a non-minimum phase behavior. Therefore, a current mode control scheme is used in this work.

Table 1. Coefficient expressions of the transfer functions (26) and (27).

Coeficient	Value
a_0	$\frac{(1-D^2)^2}{C_1C_2L_1L_2}$
a_1	$\frac{DL_1+L_2}{C_1C_2L_1L_2R}$
a_2	$\frac{C_2L_2+C_1(1-D)^2(L_1+L_2)+C_2D^2L_1}{C_1C_2L_1L_2}$
a_3	$\frac{1}{C_2R}$
b_0	$\frac{2ED(1+D^2)}{C_1C_2L_1L_2(1-D^2)R}$
b_1	$\frac{E[DL_2+C_2DR^2(1-D^4)-c_1R^2(1-D)^3(1-D^2)]}{C_1C_2L_1L_2(1-D^2)^2R^2}$
b_2	$\frac{2ED[C_1(1-D^2)+C_2}{C_1C_2L_1(1-D^2)^2R}$
b_3	$\frac{ED}{L_1(1-D^2)}$
c_0	$\frac{E(1+D^2)}{C_1C_2L_1L_2}$
c_1	$\frac{-ED^2[L_1(1+D^2)+2L_2]}{C_1C_2L_1L_2R(1-D^2)^2}$
c_2	$\frac{E[L_1(1-D)(1-D^2)+L_1D^4+L_2(1-D-D^2)]}{C_2L_1L_2(1-D^2)^2}$
c_3	$\frac{-ED(1+D)}{C_2R(1-D^2)^2}$

These transfer functions are commonly used to design control strategies, robust control analysis, tuning rules, and other design aspects aimed at future work.

3. Converter Design

Considering (13)–(16), and by setting

$$\frac{di_{L1}}{dt} = \frac{di_{L2}}{dt} = \frac{dv_{C1}}{dt} = \frac{dv_{C2}}{dt} = 0,$$

hence, the equilibrium point corresponding to the DC nominal values can be obtained as,

$$I_{L1} = \frac{ED^2}{(1-D^2)^2R}, \tag{28}$$

$$I_{L2} = \frac{ED}{(1-D^2)^2R}, \tag{29}$$

$$V_{C1} = \frac{E}{1+D}, \tag{30}$$

$$V_{C2} = \frac{ED}{1-D^2}. \tag{31}$$

Now, considering the output current as $I_O = V_{C2}/R$, current and voltage gains can be deduced as,

$$\frac{I_O}{I_{L1}} = \frac{1-D^2}{D}, \tag{32}$$

$$\frac{V_{C2}}{E} = \frac{D}{1-D^2}. \tag{33}$$

The voltage gain curve can be observed in Figure 5. Figure 6 shows the analytical waveform of the converter in a steady state. It can be observed that in mode 1 the inductors are charged and capacitors are discharged; meanwhile, in mode 2 the inductors are discharged and capacitors are charged. The form of the signals are straight lines; therefore, the voltage of inductors can be approximated by $v_L = L_1(\Delta i_L/\Delta t)$ and the current of capacitors by $i_C = C_1(\Delta v_C/\Delta t)$ where $\Delta t = DT$ in mode 1 and $\Delta t = (1-D)T$ in mode 2. Please note that T represents the switching period of the active switches, i.e., $T = 1/f_s$ where f_s is the switching frequency. Using those approximations and (1) to (8), the ripple values can be determined by,

$$\Delta i_{L1} = \frac{ED^2}{(1+D)f_sL_1}, \tag{34}$$

$$\Delta i_{L2} = \frac{ED}{(1+D)f_sL_2}, \tag{35}$$

$$\Delta v_{C1} = \frac{ED^2}{(1-D)(1+D)^2Rf_sC_1}, \tag{36}$$

$$\Delta v_{C2} = \frac{ED^2}{(1-D^2)Rf_sC_2}. \tag{37}$$

To guarantee the operation in CCM, the inductor current must never be less than or equal to zero. Therefore, the inequalities $I_{L1} - \Delta i_{L1} > 0$ and $I_{L2} - \Delta i_{L2} > 0$ must be complied. Replacing (28), (29), (34), and (35) in those inequalities, the constraint on inductors to satisfy CCM can be obtained:

$$L_1 = L_2 > \frac{(1-D)^2(1+D)R}{2f_s}. \tag{38}$$

For the selection of semiconductors, it is important to know their stress current and stress voltage values. The active switches conduct electricity in mode 1; meanwhile, diodes conduct in mode 2, as shown in Figure 4. The average current in the active switches are $I_{M1} = DI_{L2}$ and $I_{M2} = DI_{L1}$. The average current in the diodes are $I_{D1} = (1-D)I_{L2}$ and $I_{D2} = (1-D)(I_{L1} + I_{L2})$. Using the nominal DC expressions (28) and (29), the stress current are given as,

$$I_{M1} = \frac{ED^2}{(1-D^2)^2R}, \tag{39}$$

$$I_{M2} = \frac{ED^3}{(1-D^2)^2R}, \tag{40}$$

$$I_{D1} = \frac{ED}{(1-D)(1+D)^2R}, \tag{41}$$

$$I_{D2} = \frac{ED}{(1-D^2)R}. \tag{42}$$

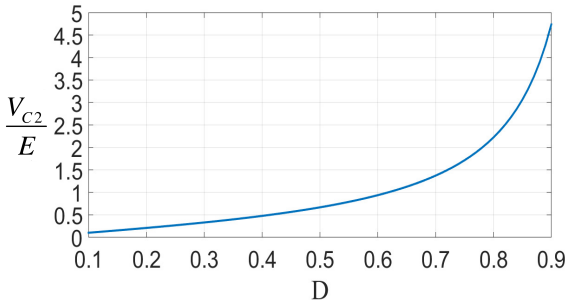

Figure 5. Voltage gain curve of the proposed converter.

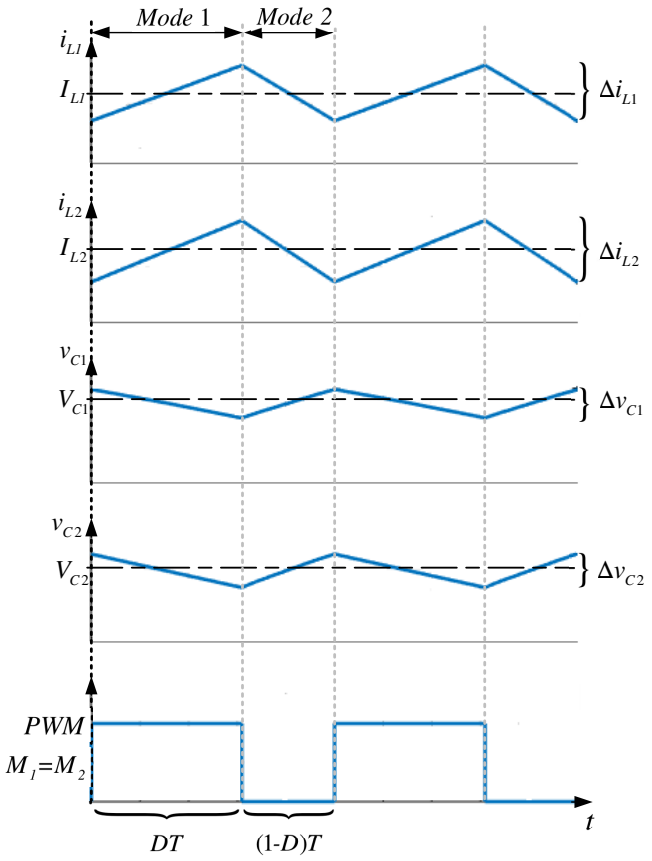

Figure 6. Steady-state waveforms of the state variables.

The active switches are opened in mode 1; meanwhile, the diodes are opened in mode 2, as shown in Figure 4a,b. The value of voltage they support are $V_{M1} = V_{C1} + V_{C2}$, $V_{M2} = V_{C2}$, $V_{D1} = V_{C1}$ and $V_{D2} = V_{C2}$. Using the nominal DC expressions (30) and (31), the stress voltages are given by

$$V_{M1} = \frac{E}{1-D^2}, \tag{43}$$

$$V_{M2} = \frac{ED}{1-D^2}, \tag{44}$$

$$V_{D1} = \frac{E}{1+D}, \tag{45}$$

$$V_{D2} = \frac{ED}{1-D^2}. \tag{46}$$

4. Controller Design

The proposed control scheme based on the average model of the system, (13)–(16), is presented. The proposal is composed of two loops: an inner current loop and an external voltage loop. Each loop results in a PI controller aimed to regulate the output voltage despite input voltage variation as commonly occurs in lithium-ion batteries. Thus, the following control objectives are established:

i. The input current i_{L1} tracks a desired current reference $x_1^*(t)$ which is calculated by the external voltage loop, as will be clear later, i.e.,

$$\lim_{t\to\infty} i_{L1}(t) = x_1^* = I_{ref}. \tag{47}$$

This is known as a current control objective.

ii. The output voltage v_{C2} follows the desired constant reference $x_4^*(t)$ on average, i.e.,

$$\lim_{t\to\infty} v_{C20}(t) = x_4^* = V_{ref}. \tag{48}$$

This objective is commonly known in DC–DC converters as the voltage regulation control objective. Notice that v_{C20} represents the average value of the output voltage v_{C2}.

The average model (13)–(16) is rewritten in a more convenient representation for control design purposes, as follows,

$$L_1\dot{x}_1 = -e - x_3 + E, \tag{49}$$

$$L_2\dot{x}_2 = -e + \zeta x_3, \tag{50}$$

$$C_1\dot{x}_3 = x_1 - \zeta x_2, \tag{51}$$

$$C_2\dot{x}_4 = u(x_1+x_2) - \frac{x_4}{R}, \tag{52}$$

where $u \triangleq (1-d)$, $e \triangleq uv_{C2}$, $x_1 \triangleq i_{L1}$, $x_2 \triangleq i_{L2}$, $x_3 \triangleq v_{C1}$, $x_4 \triangleq v_{C2}$, y $d \triangleq \zeta$. Please note that $\bar{\zeta}$ is considered to be a constant perturbation at the steady state, and it is bounded to the interval $\zeta \in [0,1]$ at all times. Then, the reference values x_i^* of each state variable in steady state can be defined as,

$$x_1^* = \bar{\zeta}x_2^*, \tag{53}$$

$$x_2^* = \frac{x_2^*}{\bar{\zeta}}, \tag{54}$$

$$x_3^* = \frac{E}{1+\bar{\zeta}}, \tag{55}$$

$$x_4^* = V_{ref}, \tag{56}$$

where V_{ref} is the reference for the desired output voltage. The error signal of each state variable can be defined as,

$$\tilde{x}_1 \triangleq x_1 - x_1^*, \tag{57}$$
$$\tilde{x}_2 \triangleq x_2 - x_2^*, \tag{58}$$
$$\tilde{x}_3 \triangleq x_3 - x_3^*, \tag{59}$$
$$\tilde{x}_4 \triangleq x_4 - x_4^*. \tag{60}$$

Additionally, the following assumptions are taken into account for control design purposes:

A1. The values of the capacitances C_1 and C_2, inductances L_1 and L_2, and the load R are unknown positive constants and may vary in steps or low over time.

A2. Decoupling assumption. The inner dynamics composed by (49)–(51) is faster than the dynamics of the output capacitor voltage. Thus, two decoupled control loops can be designed according to the time-scale separation principle: an inner current loop and an outer voltage loop.

4.1. Inner Current Loop

The decoupled assumption allows separate (49)–(51) to be used in the inner current loop, and they are written in terms of the error variables (57)–(60) as follows,

$$L_1\dot{\tilde{x}}_1 = -e - \tilde{x}_3 + E\frac{\zeta}{1+\zeta}, \tag{61}$$
$$L_2\dot{\tilde{x}}_2 = -e + \zeta\tilde{x}_3 + E\frac{\zeta}{1+\zeta}, \tag{62}$$
$$C_1\dot{\tilde{x}}_3 = \tilde{x}_1 - \zeta\tilde{x}_2. \tag{63}$$

Based on the structure (62)–(63) a PI controller is proposed on the current error $\tilde{x}_1$ to guarantee tracking of the current reference, yielding

$$e = K_{pi}\tilde{x}_1 + K_{ii}v_i, \tag{64}$$
$$\dot{v}_i = \tilde{x}_1,$$

where K_{pi} and K_{ii} are positive constants of the proportional gain and integrative gain, respectively. Please note that v_i is an auxiliary variable for the integral term. The closed-loop system yields,

$$L_1\dot{\tilde{x}}_1 = -(K_{pi}\tilde{x}_1 + K_{ii}v) - \tilde{x}_3 + E\frac{\zeta}{1+\zeta}, \tag{65}$$
$$L_2\dot{\tilde{x}}_2 = -(K_{pi}\tilde{x}_1 + K_{ii}v) + \zeta\tilde{x}_3 + E\frac{\zeta}{1+\zeta}, \tag{66}$$
$$C_1\dot{\tilde{x}}_3 = \tilde{x}_1 - \zeta\tilde{x}_2. \tag{67}$$

Please note that the proposed control scheme guarantees that the error signals tend to zero in a steady state, as follows,

$$[\tilde{x}_1, \tilde{x}_2, \tilde{x}_3, v]^\top = \left[0, 0, 0, \frac{E}{K_{ii}}\left(\frac{\zeta}{1+\zeta}\right)\right]^\top. \tag{68}$$

4.2. Outer Voltage Loop

Based on the decoupling assumption, the error states of the inner dynamic reach zero $\tilde{x}_i \to 0$, i.e., the states that compose the inner dynamic reach its reference $x_i \to x_i^*$ faster than the output capacitor voltage. Thus, (52) can be rewritten as follows,

$$C_2\dot{\tilde{z}} = EI_{ref} - \frac{2\tilde{z}}{R} - \frac{2z^*}{R}. \tag{69}$$

where a new auxiliary variable z which is defined as $z \triangleq \frac{x_4^2}{2}$. Moreover, it has been defined that $\tilde{z} = z - z^*$. Hence, a control scheme that guarantees output voltage regulation is proposed as follows,

$$\begin{aligned} I_{ref} &= -(K_{pv} v_{v1} + K_{iv} v_{v2}), \\ \tau \dot{v}_{v1} &= -v_{v1} + \tilde{z}, \\ \dot{v}_{v2} &= \tilde{z}, \end{aligned} \tag{70}$$

where K_{pv} and K_{iv} are positive design parameters; v_{v1} and v_{v2} are auxiliary variables to construct the PI controller with a limited bandwidth at proportional term which helps to avoid undesirable noise at inner control loop; and τ is a positive design term to fix the cut-off frequency of the low pass filter placed at the proportional gain of the PI controller. The controller block diagram of the current and voltage loop is shown in Figure 7.

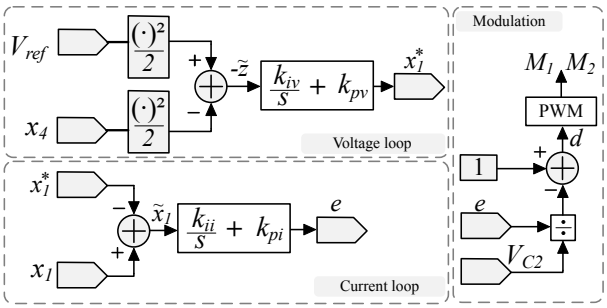

Figure 7. Controller block diagram.

5. Experimental Results

This section presents the experimental results obtained from a lab-scale prototype built in the laboratory. The experimental setup of the proposed converter is shown in Figure 8. The parameters of the converter and controller are shown in Tables 2 and 3, respectively. It is considered that the input voltage E is subjected to fluctuations in the range from 200 V to 250 V. The fluctuation emulates the behavior of a 225 V Li-ion battery pack since the range of voltage variation is very similar. The aim is to regulate this voltage range to a constant value of V_{C2} = 200 V. Thus, the load is not affected by this voltage variations of the source. The DSP TMS320F28335 (Texas Instrument Board, Dallas, TX, USA) is used to implement the control scheme shown in Figure 7. This control scheme needs to sense the input current and output voltage of the converter, which is carried out through a sensing board. The DSP reads the sensed signals and processes them into the control scheme. The PWM control signal is sent to the MOSFET drivers to fire the devices. Figure 9 shows this process in a block diagram, and Figure 10 shows the physical connections in the laboratory. To evaluate the performance of the prototype in a closed-loop, four different sets of tests are considered,

(a) steady-state proof under different loads,
(b) step-wise changes in the load,
(c) step-wise changes in the input voltage,
(d) step-wise changes in the voltage reference.

The selection of gains of both control loops is made through heuristic methods based on numerical results. The proportional gains are first selected at a minimum value. Then, they are progressively increased until the current and voltage values reach a value close to the reference. The integral gains are then progressively increased to eliminate the steady-state error. This is carried out first in the steady state test, and then its performance is observed in the step-wise changes tests. The proportional and integral gains must show

smooth transient responses with a zero steady-state error for the four different scenarios. The gains selected for this prototype are shown in Table 3.

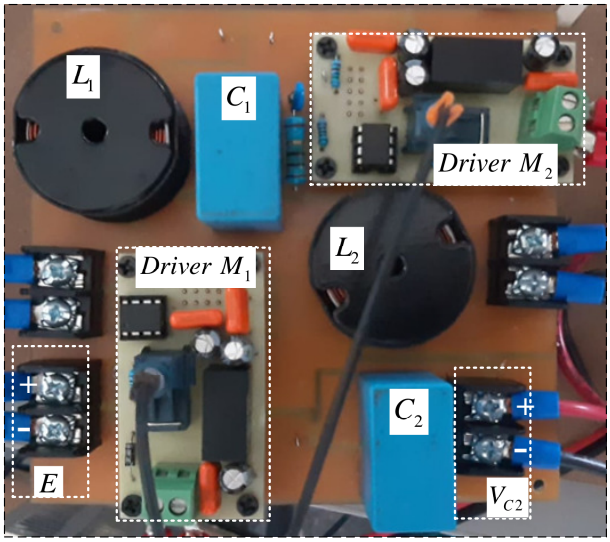

Figure 8. Experimental prototype of the proposed converter.

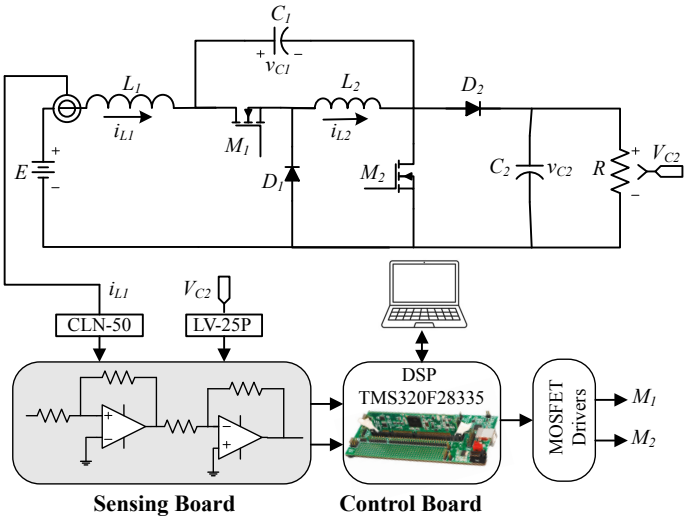

Figure 9. Block diagram of the experimental setup.

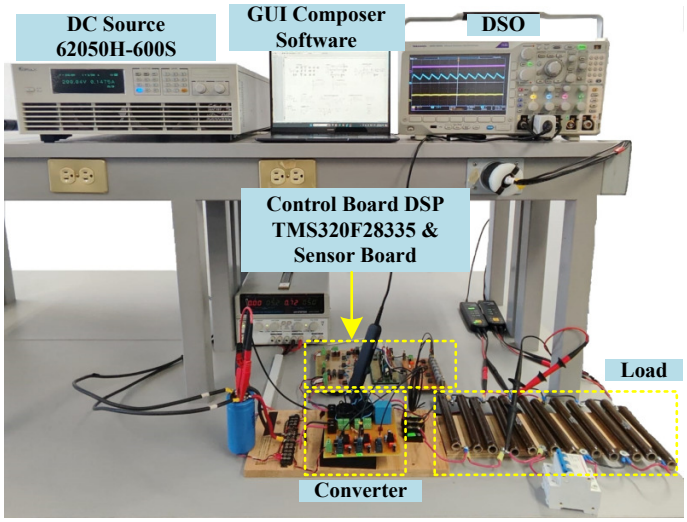

Figure 10. Experimental setup of the proposed converter at the laboratory.

Table 2. Parameters of the converter.

Parameter	Value	Part Number
Input voltage E	200 V–250 V	–
Switching frequency f_s	50 kHz	–
Reference voltage V_{ref}	200 V	–
Inductor, L_1	1.2 mH	1140–122 K
Inductor, L_2	1.2 mH	1140–122 K
Capacitor, C_1	2.2 µF	B32923C3225M000
Capacitor, C_2	2.2 µF	B32923C3225M000
MOSFET M_1	1200 V, 17 A	IPP026NIONF25
MOSFET M_2	650 V, 21 A	SCT3120ALGC11
Diode D_1 and D_2	650 V, 15 A	SCS315AHGC9
Load, R	75, 150 Ω	–

Table 3. Parameters of the controller.

Parameter	Value
Current proportional gain K_{pi}	0.5
Current integral gain K_{ii}	0.11
Voltage proportional gain K_{pv}	0.00001
Voltage integral gain K_{iv}	0.8

5.1. Steady-State Validation

This section presents the experimental responses of the state variables in steady state for two different loads considering a nominal input voltage of 200 V. The reference voltage is $V_{ref} = 200$ V. First, Figure 11 shows the experimental response with a load of 533 W corresponding to a resistor of 75 Ω. From top to bottom, this graph shows the voltage of the transfer capacitor v_{C1} with an average value of 123 V; the output voltage v_{C2} with an average value of 200 V; the input current i_{L1} with an average value of 2.8 A and a peak to peak ripple of 30 %; the current of the second inductor i_{L2} with an average value of 4.5 A with a peak to peak ripple of 30 %. As can be observed the proposed control law guarantees voltage regulation on average. Figure 12 shows the experimental response with a load of 266 W. Here, the load resistor corresponds to 150 Ω. From top to bottom, this graph shows the voltage of the transfer capacitor v_{C1} with an average value of 123 V; the output voltage v_{C2} with an average value of 200 V which is equal to the reference due to the control action; the input current i_{L1} with an average value of 1.5 A and a peak to peak ripple of 53%; the current of the second inductor i_{L2} with an average value of 2.3 A with a peak to peak ripple of 55 %.

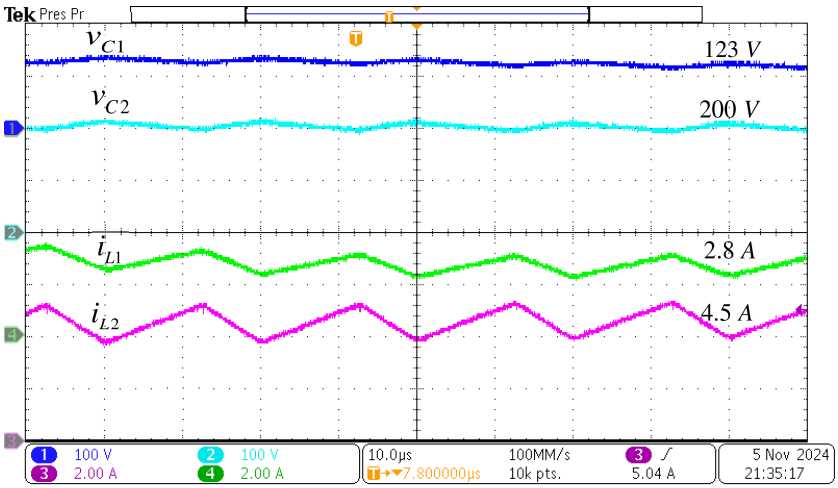

Figure 11. Experimental steady-state variables to convert an input voltage of $E = 200$ V to an output voltage of $V_{C2} = 200$ V with an output power of 533 W and a corresponding duty cycle of $D = 0.62$.

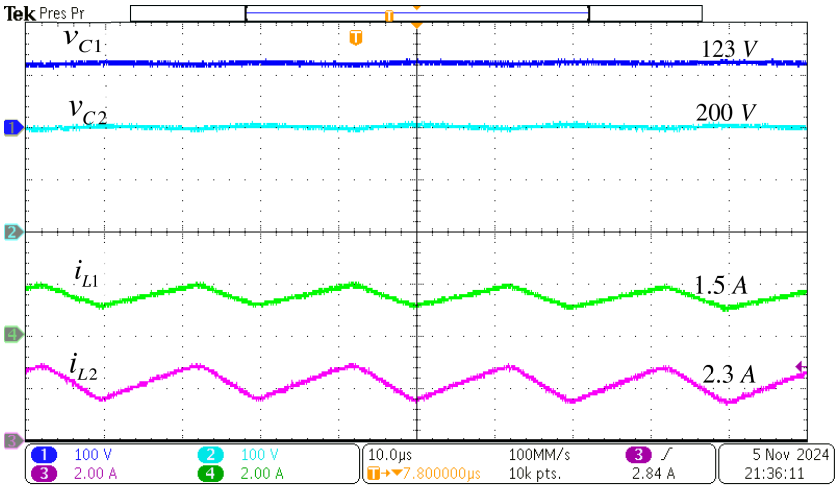

Figure 12. Experimental steady-state variables to convert an input voltage of $E = 200$ V to an output voltage of $V_{C2} = 200$ V with an output power of 266 W and a corresponding duty cycle of $D = 0.62$.

5.2. Step-Wise Changes in the Load

Step-wise changes in the load are carried out to evaluate the converter transient performance under the proposed control law. The load changes from 533 W to 266 W corresponding to resistance values of 75 Ω and 150 Ω, respectively, fixing the voltage reference to $V_{ref} = 200$ V. Figures 13 and 14 show the experimental result of this test. Figure 13 shows from top to bottom: the voltage of the transfer capacitor v_{C1} with an average value of 123 V; the output voltage v_{C2} with an average value of 200 V; the input current i_{L1} which changes from an average value of 1.5 A to an average value of 2.8 A; the current of the second inductor i_{L2} which changes from an average value of 2.3 A to an average value of 4.5 A. Additional to Figure 13, Figure 14 shows the input voltage E with a constant value of 200 V, and the output current I_O which changes from an average value from 1.33 A to an average value of 2.7 A. Both graphs illustrate how the output voltage remains regulated despite load variations. Therefore, the control law and the converter are able to fulfill the proposed control objectives.

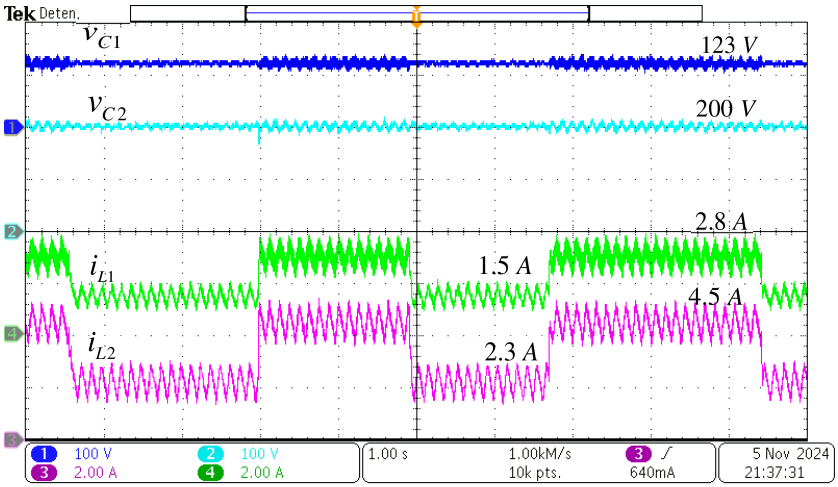

Figure 13. Experimental step-wise changes in the load from 266 W to 533 W with an output voltage regulation of $V_{C2} = 200$ V.

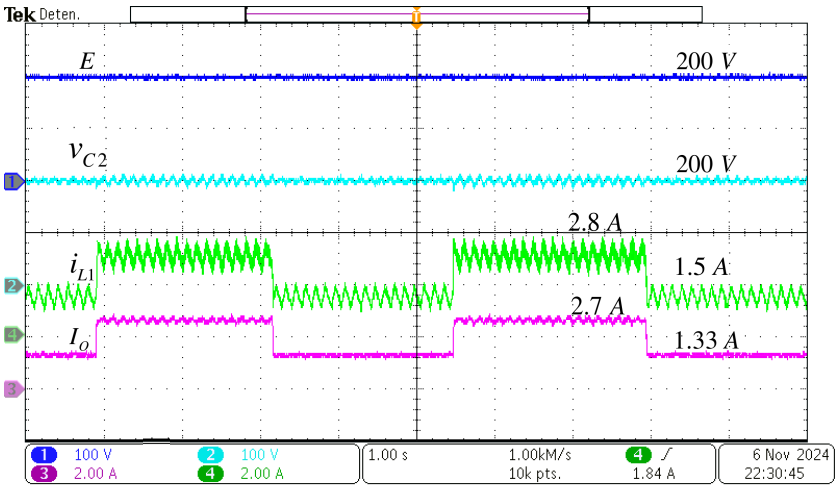

Figure 14. Experimental step-wise changes in the load from 266 W to 533 W with an output voltage regulation of $V_{C2} = 200$ V.

5.3. Step-Wise Changes in the Input Voltage

Another test to evaluate the performance of the prototype in a closed loop is to change the input voltage. It changes from 200 V to 250 V. The voltage reference is fixed to V_{ref} = 200 V as the before tests. Figure 15 shows the experimental result of this test, from top to bottom: the input voltage E with changes from 200 V to 250 V; the output voltage v_{C2} with an average value of 200 V; the input current i_{L1} which changes from an average value of 2.25 A to an average value of 2.8 A; and the output current I_O with an average value of 2.66 A. Notice that the output voltage and the output current remain constant despite input voltage variations. Thus, the performance of the controller is adequate in this test.

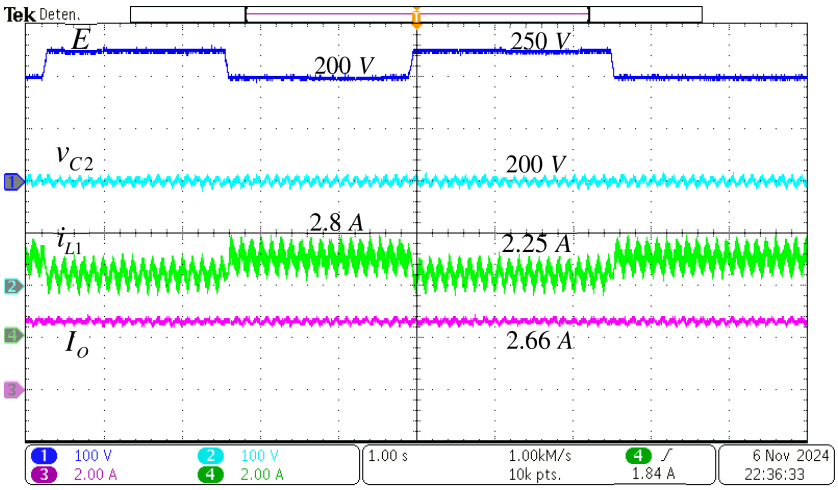

Figure 15. Experimental step-wise changes in the input voltage from 200 V to 250 V with an output voltage regulation of $V_{C2} = 200$ V and 533 W.

5.4. Step-Wise Changes in the Voltage Reference

To further verify the prototype response to regulate the output voltage on a desired reference, step-wise changes in the voltage reference from 200 V to 250 V were made. Figure 16 shows the experimental result of this test from top to bottom: the input voltage E with constant value of 200 V; the output voltage v_{C2} that adequately follows the established reference changes from 200 V to 500 V; the input current i_{L1} which changes from an average value of 1.6 A to an average value of 2.8 A; and the output current I_O which changes from

an average value of 2 A to an average value of 2.66 A. The controller exhibits excellent performance in this test.

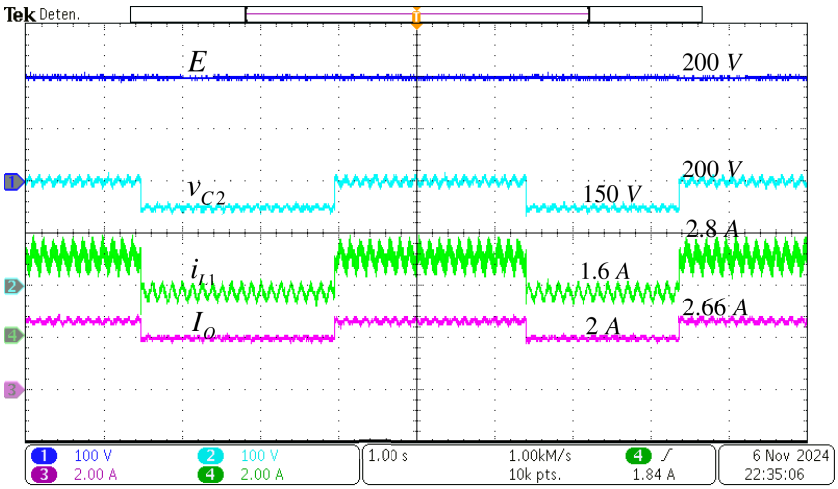

Figure 16. Experimental step-wise changes in the voltage reference from 150 V to 200 V with a constant input voltage of $E = 200$ V and a resistance load of $R = 75\ \Omega$.

5.5. Efficiency Analysis

In this subsection, an efficiency analysis is performed using the thermal module of the PSIM software. The part numbers of the semiconductor devices and other components considered in this analysis are listed in Table 2. Parasitic resistances associated with semiconductor devices and passive elements are taken into account, with their values obtained from the respective datasheets. The efficiency is calculated as follows:

$$\eta = \frac{P_{out}}{(P_{out} + P_{T,lss})}, \tag{71}$$

where $P_{T,lss}$ represents the total power losses, and P_{out} is to the output power of the converter. The efficiency is evaluated over an output power range from 50 W to 800 W. As shown in the results, the converter achieves efficiencies above 97% when operating at output power levels greater than 100 W. The peak efficiency of 97.71% is reached at 350 W, as illustrated in Figure 17. Figure 18 shows the power loss distribution of the components when the converter operates at an output power of 533 W. As observed, the diodes contribute the most to the power losses with 53% of total losses, while the MOSFETs and inductors represent 25% and 21%, respectively. Film capacitors exhibit the lowest power losses because of their low equivalent series resistance (ESR). In addition, the experimental efficiency of the proposed converter is measured. The experimental efficiency is determined by

$$\eta_{exp} = \frac{P_{out}}{P_{in}}, \tag{72}$$

where P_{in} represents the experimental input power, while P_{out} is the experimental output power of the converter. The results indicate that the converter achieves an experimental efficiency of 95% at 533 W. Based on this efficiency analysis, the proposed converter maintains efficiency levels above 95% when operating at a nominal output power of 533 W, making it a strong candidate for lithium-ion battery applications.

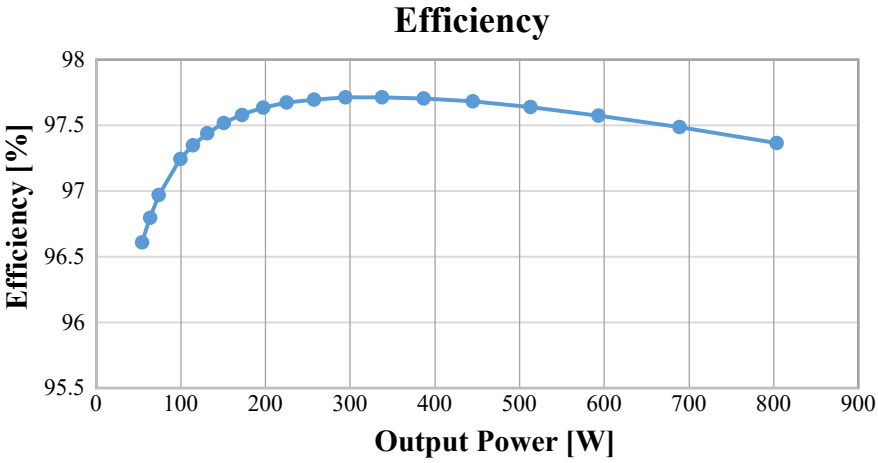

Figure 17. Efficiency of the proposed converter.

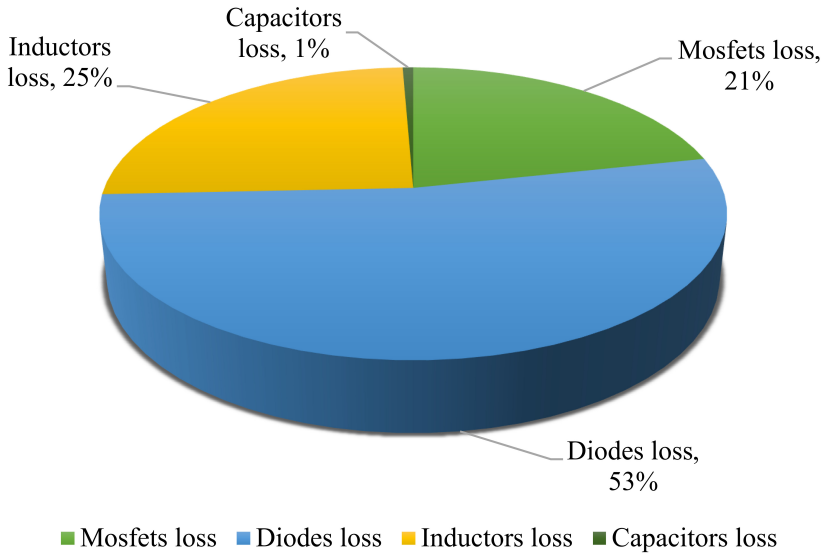

Figure 18. Power loss distribution of proposed topology at 533 W.

5.6. Comparison with Other Converters

In this subsection, the proposed converter is compared with other topologies used for a similar application. The comparison in terms of the number of components, voltage ratios, power efficiency, continuous input current, and voltage stress in semiconductors is given in Table 4. The better efficiency of the topologies is presented in the converter of [11], in the converter of [12], and in the converter proposed in this work. Please note that the proposed converter is assessed at higher loads compared to the other topologies presented in Table 4. Also, most of the compared topologies replace diodes with switches, increasing the complexity of the topologies in contrast to the proposal. On the other hand, the proposed converter and converters presented in [11,14] have a non-pulsating input current. That feature is beneficial for battery-discharge applications. However, it can be observed that the proposed converter has a high number of components and high voltage stress in the semiconductors. Finally, the power managed for the proposed converter is higher than the others in the performed comparison.

Table 4. Comparison between proposed converter and other converters.

Converter	**Proposed**	[10]	[11]	[12]	[13]	[14]
Switches	2	4	6	4	4	2
Diodes	2	0	0	0	0	2
Inductors	2	1	1	1	1	2
Capacitors	2	1	3	2	1	2
Voltage Gain	$D/(1-D^2)$	$D/(1-D)$	$D/(1.5-D)$	$D/(1-D)$	$D/(1-D)$	$D/(1-D)$
Efficiency	95%	86%	95.63%	96.5%	90.7%	90.5%
P_{out}	533 W	16.5 W	2.38 W	6.8 W	4.32 W	500 W
f_s	50 kHz	1000 kHz	1000 kHz	1000 kHz	1000 kHz	100 kHz
Non-pulsating input current						
Continuous current	Yes	No	Yes	No	No	Yes
Voltage Stress of Switches						
Voltage level 1	$E/(1-D^2)$	E	$ED/2(1.5-D)$	E	E	$E/(1-D)$
Voltage level 2	$ED/(1-D^2)$	$ED/(1-D)$	$ED/(1.5-D)$	$ED/(1-D)$	$ED/(1-D)$	
Voltage Stress of Diodes						
Voltage level 1	$E/(1+D)$	–	–	–	–	$E/(1-D)$
Voltage level 2	$ED/(1-D^2)$					

6. Conclusions

In this paper, the design and control step-up/step-down converter with non-pulsating input current and non-inverter output voltage were detailed. An analysis of the proposed converter was carried out in such a way that design expressions were obtained for a correct selection of passive components. In addition, mathematical models that describe the dynamics of the converter were obtained. Based on the modeling, a two-loop control scheme was proposed. Afterward, it was described how to derive the control law of each loop. To validate the design expressions and control scheme, a 533 W prototype was built in the laboratory. The steady-state experimental results validated the ripple and average expressions of the state variables. It was noted that the full load efficiency of the converter is 95%. Tests at step-wise load changes, step-wise changes in the input voltage, and step-wise changes in the voltage reference validated the correct design of the controller, obtaining smooth transient responses with a zero steady-state error. Through a wide set of experimental results, the capability of the converter to regulate the output voltage to the desired reference despite disturbances. The advantages of the proposed converter of having the ability to step up and step down the voltage, continuous input current, and being a non-cascade structure with high efficiency make it suitable for the application of discharge voltage regulation in lithium-ion batteries. In addition, having a non-inverted output voltage and a low number of active switches make it easy to implement and control. However, according to a comparison with other converters used in similar applications, it has more components and high-stress voltage on the semiconductors. Nevertheless, the large number of components is compensated with a smaller size of them. Notice that the proposed converter is assessed in an academic prototype; this type of application is mainly aimed at battery voltage regulation in the range of less than 1 kW. However, if the power rating is increased, the converter elements, semiconductors, and energy storage elements will be designed according to the guidelines proposed in Section 3.

Author Contributions: Conceptualization, J.A.V.-L. and P.R.M.-R.; methodology, J.A.V.-L., P.R.M.-R., D.L.-C. and C.J.R.-C.; software, J.A.V.-L. and C.J.R.-C.; validation, J.A.V.-L. and C.J.R.-C.; formal analysis, J.A.V.-L., P.R.M.-R., D.L.-C. and C.J.R.-C.; investigation, J.A.V.-L., P.R.M.-R., D.L.-C., C.J.R.-C., Á.H.-G. and D.G.; resources, Á.H.-G. and D.G.; data curation, Á.H.-G. and D.G.; writing—original draft preparation, J.A.V.-L., P.R.M.-R., D.L.-C., C.J.R.-C., Á.H.-G. and D.G.; writing—review and editing, J.A.V.-L., P.R.M.-R., D.L.-C., C.J.R.-C., Á.H.-G. and D.G.; visualization, J.A.V.-L., P.R.M.-R., D.L.-C., C.J.R.-C., Á.H.-G. and D.G.; supervision, J.A.V.-L. and P.R.M.-R.; project administration, J.A.V.-L. and P.R.M.-R.; funding acquisition, Á.H.-G. and D.G. All authors have read and agreed to the published version of the manuscript.

Funding: This research supported by SECIHTI, Mexico, which supports this work through the program "Estancias Posdoctorales por México Convocatoria 2023, No. 5898007".

Data Availability Statement: The original contributions presented in this study are included in the article. Further inquiries can be directed to the corresponding author.

Conflicts of Interest: The authors declare no conflicts of interest.

Abbreviations

The following abbreviations are used in this manuscript:

DC–DC	Direct current to direct current
DC	Direct current
DC–AC	Direct current to alternating current
PFC	Power factor correction
LED	Light-emitting diode
UPS	Uninterruptible power supply
PV	Photovoltaic
SEPIC	Single-ended primary inductor converter

References

1. Gholizadeh, H.; Gorji, S.A.; Sera, D. A Quadratic Buck-Boost Converter with Continuous Input and Output Currents. *IEEE Access* **2023**, *11*, 22376–22393. [CrossRef]
2. Sarikhani, A.; Allahverdinejad, B.; Hamzeh, M. A Nonisolated Buck–Boost DC–DC Converter with Continuous Input Current for Photovoltaic Applications. *IEEE J. Emerg. Sel. Top. Power Electron.* **2021**, *9*, 804–811. [CrossRef]
3. Monteiro, J.; Pires, V.F.; Foito, D.; Cordeiro, A.; Silva, J.F.; Pinto, S. A Buck-Boost Converter with Extended Duty-Cycle Range in the Buck Voltage Region for Renewable Energy Sources. *Electronics* **2023**, *12*, 584. [CrossRef]
4. Liu, X.; Liu, W.; He, M.; Wang, W.; Zhou, Q.; Xu, J. Boost-Type Single-Stage Step-Down Resonant Power Factor Correction Converter. *IEEE Trans. Ind. Electron.* **2021**, *68*, 8081–8092. [CrossRef]
5. Chang, Y.; Yu, W.; Luo, M.; Zhou, F.; Huang, W.; Zhai, G. Anti-Interference Control Method of Buck–Boost Converter Based on High-Order Nonlinear Disturbance Observer. *Electronics* **2024**, *13*, 1318. [CrossRef]
6. Rivera, S.; Flores-Bahamonde, F.; Renaudineau, H.; Dragicevic, T.; Kouro, S. A Buck-Boost Series Partial Power Converter using a Three-Port Structure for Electric Vehicle Charging Stations. In Proceedings of the 2021 IEEE 12th Energy Conversion Congress and Exposition-Asia (ECCE-Asia), Singapore, 24–27 May 2021; pp. 1749–1754. [CrossRef]
7. Obregón-Pulido, G.; Solís-Perales, G.; Meda-Campaña, J.A.; Munguia, R. Exact Sinusoidal Signal Tracking on a Modified Topology of Boost and Buck-Boost Converters. *Electronics* **2024**, *13*, 793. [CrossRef]
8. Chen, X.; Pise, A.A.; Elmes, J.; Batarseh, I. Ultra-Highly Efficient Low-Power Bidirectional Cascaded Buck-Boost Converter for Portable PV-Battery-Devices Applications. *IEEE Trans. Ind. Appl.* **2019**, *55*, 3989–4000. [CrossRef]
9. Tekin, H.; Setrekli, G.; Murtulu, E.; Karşıyaka, H.; Ertekin, D. A Proposed Single-Input Multi-Output Battery-Connected DC–DC Buck–Boost Converter for Automotive Applications. *Electronics* **2023**, *12*, 4381. [CrossRef]
10. Tsai, Y.Y.; Tsai, Y.S.; Tsai, C.W.; Tsai, C.H. Digital Noninverting-Buck–Boost Converter With Enhanced Duty-Cycle-Overlap Control. *IEEE Trans. Circuits Syst. II Express Briefs* **2017**, *64*, 41–45. [CrossRef]
11. Mishra, A.; Zhu, W.; Wicht, B.; Smedt, V.D. An All-1.8-V-Switch Hybrid Buck–Boost Converter for Li-Battery-Operated PMICs Achieving 95.63% Peak Efficiency Using a 288-m DCR Inductor. *IEEE Trans. Power Electron.* **2023**, *38*, 3444–3454. [CrossRef]

12. Ju, Y.M.; Shin, S.U.; Huh, Y.; Park, S.H.; Bang, J.S.; Kim, K.D.; Choi, S.W.; Lee, J.H.; Cho, G.H. 10.4 A hybrid inductor-based flying-capacitor-assisted step-up/step-down DC-DC converter with 96.56% efficiency. In Proceedings of the 2017 IEEE International Solid-State Circuits Conference (ISSCC), San Francisco, CA, USA, 5–9 February 2017; pp. 184–185. [CrossRef]
13. Rao, S.; Khan, Q.; Bang, S.; Swank, D.; Rao, A.; McIntyre, W.; Hanumolu, P.K. A 1.2-A Buck-Boost LED Driver With On-Chip Error Averaged SenseFET-Based Current Sensing Technique. *IEEE J.-Solid-State Circuits* **2011**, *46*, 2772–2783. [CrossRef]
14. Villanueva-Loredo, J.A.; Ortiz-Lopez, M.G.; Leyva-Ramos, J.; Diaz-Saldierna, L.H. Switching Regulator Based on a Non-Inverting Step-Down/Up DC–DC Converter for Lithium-Ion Battery Applications. *Micromachines* **2023**, *14*, 1144. [CrossRef] [PubMed]
15. Brand, M.J.; Hofmann, M.H.; Schuster, S.S.; Keil, P.; Jossen, A. The Influence of Current Ripples on the Lifetime of Lithium-Ion Batteries. *IEEE Trans. Veh. Technol.* **2018**, *67*, 10438–10445. [CrossRef]
16. Martin, A.D.; Cano, J.M.; Silva, J.F.A.; Vázquez, J.R. Backstepping Control of Smart Grid-Connected Distributed Photovoltaic Power Supplies for Telecom Equipment. *IEEE Trans. Energy Convers.* **2015**, *30*, 1496–1504. [CrossRef]
17. Ganesh, V.S.; Singha, A.K. Design of Stable Digital V2 Controllers for the Synchronous Noninverting Buck–Boost Converter. *IEEE J. Emerg. Sel. Top. Power Electron.* **2023**, *11*, 2826–2836. [CrossRef]
18. Chen, C.; Liu, J.; Lee, H. A 2-MHz 9–45-V Input High-Efficiency Three-Switch ZVS Step-Up/-Down Hybrid Converter. *IEEE J.-Solid-State Circuits* **2021**, *56*, 855–865. [CrossRef]
19. Mohammadi, M.R.; Amoorezaei, A.; Khajehoddin, S.A.; Moez, K. A High Step-Up/Step-Down LVS-Parallel HVS-Series ZVS Bidirectional Converter with Coupled Inductors. *IEEE Trans. Power Electron.* **2022**, *37*, 1945–1961. [CrossRef]
20. Akhormeh, A.R.N.; Abbaszadeh, K.; Moradzadeh, M.; Shahirinia, A. High-Gain Bidirectional Quadratic DC–DC Converter Based on Coupled Inductor with Current Ripple Reduction Capability. *IEEE Trans. Ind. Electron.* **2021**, *68*, 7826–7837. [CrossRef]
21. Krein, P. *Elements of Power Electronics*; Oxford Series in Electrical and Computer Engineering; Oxford University Press: Oxford, UK, 2014.
22. Zhang, Y.; Yang, G.; He, X.; Elshaer, M.; Perdikakis, W.; Li, H.; Yao, C.; Wang, J.; Zou, K.; Xu, Z.; et al. Leakage Current Issue of Non-Isolated Integrated Chargers for Electric Vehicles. In Proceedings of the 2018 IEEE Energy Conversion Congress and Exposition (ECCE), Portland, OR, USA, 23–27 September 2018; pp. 1221–1227. [CrossRef]
23. Zogogianni, C.G.; Tatakis, E.C.; Vekic, M.S. Non-Isolated Reduced Redundant Power Processing DC/DC Converters: A Systematic Study of Topologies with Wide Voltage Ratio for High-Power Applications. *IEEE Trans. Power Electron.* **2019**, *34*, 8491–8502. [CrossRef]

Disclaimer/Publisher's Note: The statements, opinions and data contained in all publications are solely those of the individual author(s) and contributor(s) and not of MDPI and/or the editor(s). MDPI and/or the editor(s) disclaim responsibility for any injury to people or property resulting from any ideas, methods, instructions or products referred to in the content.